

Article

Improved Transient Performance of a DFIG-Based Wind-Power System Using the Combined Control of Active Crowbars

Muhammad Arif Sharafat Ali 

Independent Researcher, Multan 60000, Pakistan; sharafat@skku.edu

Abstract: A significant electromotive force is induced in the rotor circuit of a doubly fed induction generator (DFIG) due to its high vulnerability to grid faults. Therefore, the system performance must be increased with appropriate control actions that can successfully offset such abnormalities in order to provide consistent and stable operations during grid disturbances. In this regard, this paper presents a solution based on a combination of an energy storage-based crowbar and a rotor-side crowbar that makes the effective transient current and voltage suppression for wind-driven DFIG possible. The core of the solution is its ability to restrict the transient rotor and stator overcurrents and DC-link overvoltages within their prescribed limits, thereby protecting the DFIG and power converters and improving the system's ability to ride through faults. Further, the capacity of an energy storage device for transient suppression is estimated. The results confirmed that the proposed approach not only kept the transient rotor and stator currents within $\pm 50\%$ of their respective rated values in severe system faults but also limited the DC-link voltage variations under $\pm 15\%$ of its rated value, achieving transient control objectives precisely and maintaining a stable grid connection during the faults.

Keywords: wind turbine system; doubly fed induction generator; low-voltage ride-through; active crowbars



Citation: Ali, M.A.S. Improved Transient Performance of a DFIG-Based Wind-Power System Using the Combined Control of Active Crowbars. *Electricity* **2023**, *4*, 320–335. <https://doi.org/10.3390/electricity4040019>

Academic Editor: François Auger

Received: 29 August 2023

Revised: 27 October 2023

Accepted: 13 November 2023

Published: 14 November 2023



Copyright: © 2023 by the author. Licensee MDPI, Basel, Switzerland. This article is an open access article distributed under the terms and conditions of the Creative Commons Attribution (CC BY) license (<https://creativecommons.org/licenses/by/4.0/>).

1. Introduction

The massive integration of wind power is increasing globally since there is a growing demand in meeting electrical energy requirements with renewable energy sources. However, it has opened up new study fields in terms of the successful integration of wind-power plants (WPPs) into the electrical power network [1,2], stable system operations [3,4], and grid assistance during transients [5,6]. Thus, better system security is possible if the WPPs remain attached to the grid during grid disturbances and assist transient voltage suppression. As a result, many electricity companies have been forced to revise their grid codes. The main concern among them is the successful implementation of the low-voltage ride-through (LVRT) ability of the wind-power systems [5].

Since the variable-speed concept emerged in WT operations [6], significant developments in high efficiency and reliability have been achieved. Presently, doubly fed induction generators (DFIGs) are the widespread choice for wind-turbine-generators (WTGs) due to their flexible speed operation, high efficiency, and low-rating converters [7]. A DFIG is highly prone to grid disturbances because of its direct connection to the grid via its stator circuit. Due to low-rated rotor-side converter (RSC) and DC-link voltage restrictions, the rotor circuit experiences a significant electromotive force (EMF) during faults [8]. Thus, it is anticipated that the wind-power converters (i.e., RSC and grid-side converter (GSC)) will experience overcurrents, resulting in transient overvoltages in the DC circuit that connects them.

Exhaustive efforts have been made to ensure this, and several solutions have been developed to boost the LVRT potential of DFIG-based wind-energy conversion systems (WECSs). A critical analysis of the start-of-the-art techniques proposed for the successful

handling of LVRT is presented. The conventional vector controls are incapable of properly controlling the DFIGs under grid faults because a sizable EMF caused by voltage dips may initiate substantial transient currents in the RSC and the DFIG. With typical vector controls, the stator natural flux caused by grid-voltage dips declines sluggishly, thus lengthening the transient process.

Several studies are available in the literature that provided various technical solutions for dealing with the power-system stability problems and improving the LVRT capability of DFIG-based WECSs. These solutions are broadly classified into two subgroups: (1) improved control structures for DFIGs and (2) enhanced external hardware-based solutions. Numerous modified control schemes have been presented in [7,9–20], such as feedforward current-references control [7], flux linkage control [9], demagnetization control [10], modified controls for RSC [11], flux magnitude and angle control [12], sliding-mode control [13,14], negative-sequence current regulation [15], an enhanced reactive power support [16], and an improved control design for wind-power converters [17]. A double impedance–substitution control approach to expanding the LVRT capability of a DFIG was suggested in [18]. A study of the transient stability of DFIG-based WT systems was presented in [19], in which a phase-locked loop and current control loops were considered. Lyapunov’s methods were used to examine the stability of the system. The authors of [20] proposed a method for alleviating the negative effects of transient rotor currents and stator voltages on DFIG during grid disturbances using feedforward control loops. The improved WTG controls were effective in suppressing the transient currents and voltages of the DFIG and the power converters, as well as accelerating the flux-decaying process to shorten the transient phenomenon.

Modern WTs mostly include assisting hardware, such as crowbar protection [8,21,22], to mitigate DC-link voltage variations. Presently, the application of fault-current limiters (FCLs), such as an inductive bridge-type FCL [23] and a capacitive bridge-type FCL [5,24–26], has attracted special attention as a potential solution for LVRT enhancement. Other hardware applications, such as a STATCOM [27], an energy storage device (ESD) [22,28], and a dynamic voltage restorer [29], have also been recommended. To overwhelm the negative-sequence voltage during faults, the authors of [30] developed a control scheme based on an active voltage equalization dynamic control. In [31], an analytical method based on the fault current characteristics was established to handle the ride-through capability of DFIG, and a switching mechanism between the RSC control and crowbar was proposed.

Large transient rotor overcurrents are generated under serious grid faults, which also flow into the DC-link, rendering the DFIG uncontrollable. The decoupled control of the RSC and GSC may be destroyed by the DC-link voltage fluctuations. Furthermore, large fluctuations in the electromagnetic torque will originate. These undesirable effects may cause mechanical and electrical components to fail, be disastrous for safe system operation, and worsen the power quality.

To successfully accommodate the massive integration of wind energy, appropriate changes in the system and its control mechanism are required. Concerning this, the authors intended to establish a control design based on active crowbars, embedded in the WTG controls, which can improve the system performance during transient conditions and ensure stability and quality operations.

The ultimate objectives of this study and the proposed technical solutions for achieving them can be classified into two sets, which are briefly stated as follows: Enhancing the LVRT operation of a DFIG by developing control schemes based on auxiliary crowbar controls. To limit the transient rotor currents, an active crowbar at the rotor-side is designed, in which a set of resistors is paralleled with a rotor circuit breaker (RCB) and connected to the RSC. At the DC-link, an ESD-based crowbar is proposed and inserted in parallel to it. The proposed combined control scheme of active crowbars successfully enhanced the DC-link behavior in the support grid during faults.

The main contributions of this study are as follows:

- Efficient and effective control schemes based on active crowbar controls were designed to cater to the transient effects of rotor current, stator current, and DC-link voltage throughout grid instabilities, thereby strengthening the LVRT capability of the DFIG and improving the transient performance of the system.
- The simple control design of the proposed scheme makes it attractive for enhancing the transient performance of the system when compared to other hardware-based solutions in terms of complexity and cost.
- The proposed method is a promising solution for realizing the LVRT capability, owing to its ability to mitigate the transient effects in generator electromagnetic torque. Moreover, the proposed design is suitable for wind-energy systems due to its practical implementation.

The rest of the paper is organized into seven sections. A basic explanation of the wind-driven DFIG system is presented in Section 2. A comprehensive mathematical modeling and analysis of a DFIG are reviewed in Section 3. In Section 4, an exhaustive mathematical formulation, designed procedures, and evaluations of the proposed control schemes are provided. The capacity estimation of ESD required for LVRT is provided in Section 5. To examine the performances of the proposed control schemes, simulation studies for a 1.5 MW DFIG system are presented and addressed in Section 6. Further, a comparison of the proposed scheme with the DC-chopper is performed. Finally, the paper is concluded in Section 7.

2. Overview of a DFIG-WT System

A comprehensive diagram of a DFIG-based WT system is shown in Figure 1. It comprises a WT, a DFIG, a coupling transformer, an RSC, a DC-link circuit, a GSC, and an allied control structure.

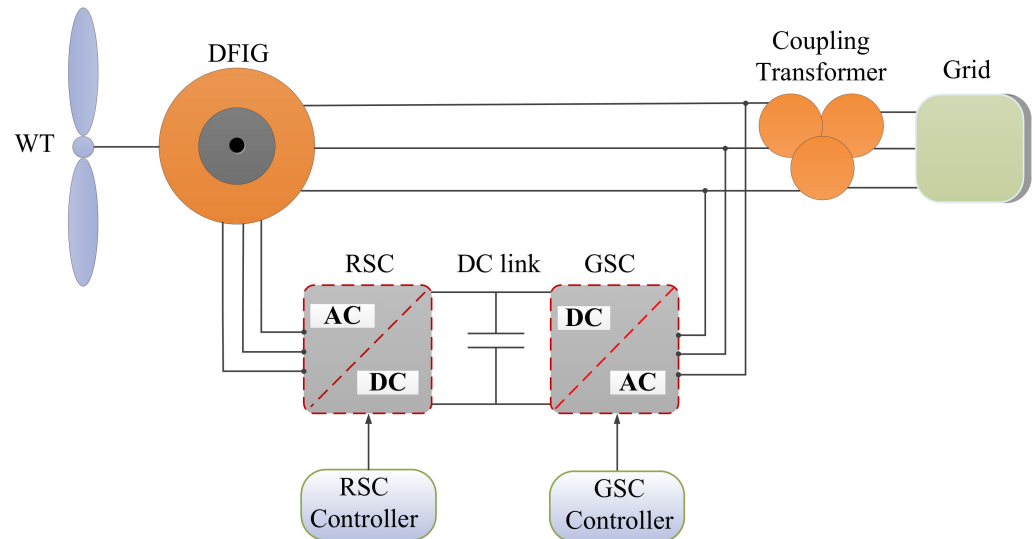


Figure 1. Overall diagram of a DFIG-based WECS.

As previously mentioned, the stator winding of a DFIG is directly coupled to the grid through a transformer, whereas the rotor winding is indirectly connected via power-electronics converters.

3. Modeling and Analysis of a DFIG

Before discussing the proposed scheme designed for suppressing transient currents and voltages and improving the LVRT capability of the DFIG, it is advantageous to establish the key aspects of the DFIG's modeling and to emphasize both its steady-state and transient behaviors from the control point of view.

3.1. DFIG Dynamical Model

The dynamical behavior of a DFIG under steady-state conditions is investigated using Park's transformation, and for convenience, all parameters are stated for the stator side [23]. For both stator- and rotor-current space vectors, the motor convention is used. A synchronous reference frame (SRF) is used to describe the dynamical model of a DFIG, and the formulations for voltage and flux linkages, expressed as complex vectors, are described [32–34].

$$\vec{v}_s = R_s \vec{i}_s + \frac{d}{dt} \vec{\psi}_s + j\omega_s \vec{\psi}_s \quad (1a)$$

$$\vec{v}_r = R_r \vec{i}_r + \frac{d}{dt} \vec{\psi}_r + j(\omega_s - \omega_r) \vec{\psi}_r \quad (1b)$$

$$\vec{\psi}_s = L_s \vec{i}_s + L_m \vec{i}_r \quad (2a)$$

$$\vec{\psi}_r = L_r \vec{i}_r + L_m \vec{i}_s \quad (2b)$$

$$L_s = L_{ls} + L_m, \quad L_r = L_{lr} + L_m, \quad \omega_{sl} = \omega_s - \omega_r \quad (3)$$

where v_s and v_r are the stator and rotor voltages, respectively; i_s and i_r are the stator and rotor currents, respectively; ψ_s and ψ_r are the stator flux linkage and rotor flux linkage, respectively; R_r is the rotor resistance; L_s and L_r are the stator and rotor inductances, respectively; L_{ls} and L_{lr} are the stator- and rotor-leakage inductances, respectively; and ω_s , ω_r , and ω_{sl} are the electrical angular frequency, rotor angular frequency, and slip frequency, respectively.

The stator winding resistance (R_s), which is usually negligible in large-scale grid-connected DFIGs, can be neglected. The stator voltage Equation (1a) consequently becomes

$$\vec{v}_s = \frac{d}{dt} \vec{\psi}_s + j\omega_s \vec{\psi}_s \quad (4)$$

According to Equation (4), the stator voltage predominantly determines the stator flux linkage. Now, a direct relation between stator and rotor fluxes is developed. In this context, from Equation (2a),

$$\vec{i}_s = \frac{\vec{\psi}_s - L_m \vec{i}_r}{L_s} \quad (5)$$

Substituting Equation (5) into Equation (2b), the expression for the rotor flux linkage is

$$\vec{\psi}_r = \frac{L_m}{L_s} \vec{\psi}_s + \sigma L_r \vec{i}_r, \quad \sigma = 1 - \frac{L_m^2}{L_s L_r} \quad (6)$$

In Equation (6), σ is the leakage coefficient. The rotor voltage (1b) in the SRF can also be expressed as

$$\vec{v}_r = \underbrace{\frac{L_m}{L_s} \left(\frac{d}{dt} \vec{\psi}_s + j\omega_s \vec{\psi}_s \right)}_{\vec{e}_r} + \underbrace{R_r \vec{i}_r + \sigma L_r \left(\frac{d}{dt} + j\omega_s \right) \vec{i}_r}_{\vec{U}_{RL}} \quad (7)$$

From Equation (7), it is clear that the rotor voltage can be separated into two terms: (1) e_r , which is the rotor EMF caused by the stator flux linkage, and (2) U_{RL} , which is the voltage drop across the rotor transient inductance (σL_r) and the rotor resistance. Based on (7), it is possible to realize the equivalent model of the DFIG from the rotor-side, which is illustrated in Figure 2.

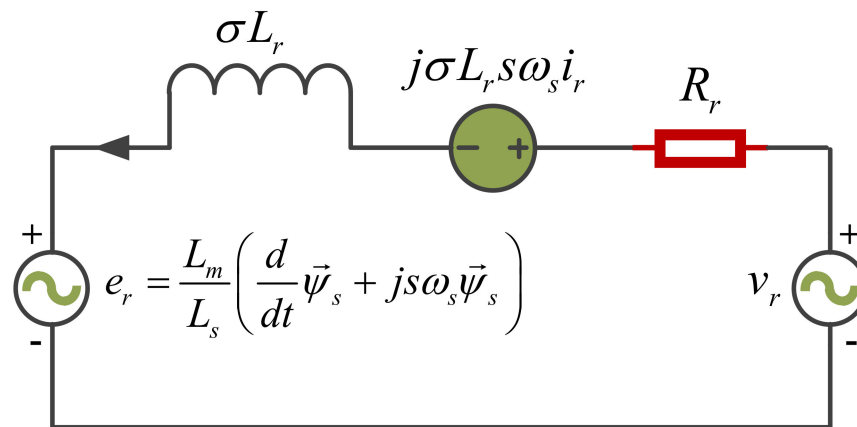


Figure 2. Equivalent model of a DFIG from the rotor side.

3.2. Steady-State Analysis of the DFIG

Since the stator flux linkage in the SRF is constant, the transient process of the flux under normal operating conditions can be ignored. As a result, the rotor EMF can be reduced to

$$\vec{e}_r = \frac{L_m}{L_s} j s \omega_s \vec{\psi}_s \tag{8}$$

From Equation (4), the analytical expression for the stator voltage will be given by

$$\vec{v}_s = j \omega_s \vec{\psi}_s \tag{9}$$

Putting Equation (9) into Equation (8),

$$\vec{e}_r = \frac{L_m}{L_s} s \vec{v}_s \tag{10}$$

The amplitude of the rotor EMF is given by

$$|E_r| = \frac{L_m}{L_s} s V_s \tag{11}$$

Here, V_s is the rated stator voltage. From Equation (11), it is clear that e_r is proportional to slip (s), which varies between -0.3 and 0.3 [35]. According to Equation (11), it is obvious that the rotor EMF amplitude under normal conditions is quite small and, at most, 30% of the specified stator voltage. Thus, it will provide about 30% of the output of the generator rating; however, some safety margin must also be considered.

3.3. Transient Analyses of the DFIG

This subsection discusses the transient analyses of a DFIG under grid faults (i.e., symmetrical and asymmetrical). Following a grid disturbance, the stator flux can be decomposed as:

$$\vec{\psi}_s = \vec{\psi}_{sp} + \vec{\psi}_{sn} + \vec{\psi}_{sdc} \tag{12}$$

In Equation (12), $\vec{\psi}_{sp}$, $\vec{\psi}_{sn}$, and $\vec{\psi}_{sdc}$ represent the positive-sequence, negative-sequence, and transient components, respectively, of the stator flux linkage.

3.3.1. Symmetrical Grid Faults

The stator flux linkage will include a transient component in the case of a symmetrical fault, which is given by

$$\vec{\psi}_s = \underbrace{\frac{(1-d)V_s}{j\omega_s}}_{\vec{\psi}_{sp}} + \underbrace{\frac{dV_s}{j\omega_s} e^{-t/\tau_s} e^{-j\omega_s t}}_{\vec{\psi}_{sdc}} \quad (13)$$

In Equation (13), d is the voltage dip level and $\tau_s (=L_s/R_s)$ is designated by the stator time constant of the flux linkage. Equation (13) can be decomposed into two terms: Ψ_{sp} and Ψ_{sdc} , which decay with τ_s . The Ψ_{sn} will not exist in cases with a symmetrical fault. The transient rotor EMF generated by the stator flux under symmetrical faults can now be represented by Equation (8).

$$\vec{e}_r = \frac{L_m}{L_s} \left[s(1-d)V_s - (1-s)dV_s e^{-t/\tau_s} e^{-j\omega_s t} \right] \quad (14)$$

It is obvious that the preliminary magnitude of the transient EMF during grid faults is comparatively larger than its normal value. Thus, the maximum amplitude of the transient rotor EMF is given by

$$|E_r|_{\max} = \frac{L_m}{L_s} V_s [|s|(1-d) - (1-s)d] \quad (15)$$

Considering the most serious scenario of a maximum voltage dip ($d = 1$) and $s = -0.3$, the starting strength of the rotor EMF during symmetrical faults can be approximated using Equation (16):

$$|E_r|_{\max-sym} \approx 1.3 \frac{L_m}{L_s} V_s \quad (16)$$

which is several times higher than its normal value and far exceeds the DC-link voltage from its rated value. The DC-link voltage will continue to surpass during serious grid voltage dips unless the ψ_{sdc} does not decay to a specific extent.

3.3.2. Asymmetrical Grid Faults

Based on the above analysis, it is understood that the stator affects the dynamic behavior of the rotor by injecting an EMF by the stator flux linkage. The stator flux linkage will also have negative-sequence components in cases with asymmetrical faults. By expanding Equation (12),

$$\vec{\psi}_s = \frac{V_{sp}}{j\omega_s} e^{j\omega_s t} + \frac{V_{sn}}{-j\omega_s} e^{-j\omega_s t} + \psi_{sdc} e^{-t/\tau_s} \quad (17)$$

In Equation (17), V_{sp} and V_{sn} represent the amplitudes of the positive- and negative-sequence components of the stator voltage, respectively. The value of Ψ_{sdc} is determined by the angle ($\varphi\Psi_0$) between the Ψ_{sp} and Ψ_{sn} . The initial DC flux for asymmetrical grid faults differs from that for symmetrical grid faults in that it is determined by the fault type and the time of occurrence. This induced DC component has the maximum value for $\varphi\Psi_0 = \pi$, and there is no DC component if $\varphi\Psi_0 = 0$. By transforming Equation (17) into the stationary rotor-reference frame,

$$\vec{\psi}_s^r = \frac{V_{sp}}{j\omega_s} e^{js\omega_s t} + \frac{V_{sn}}{-j\omega_s} e^{-j(2-s)\omega_s t} + \psi_{sdc} e^{-t(\frac{1}{\tau_s} + j\omega_r)} \quad (18)$$

From Equation (18), the expression of the rotor EMF can be substituted as:

$$\vec{e}_r^r = \frac{L_m}{L_s} \frac{d}{dt} \vec{\psi}_s^r = \frac{L_m}{L_s} \left[sV_{sp}e^{j\omega_s t} + (2-s)V_{sn}e^{-j(2-s)\omega_s t} - \left(\frac{1}{\tau_s} + j\omega_r \right) \vec{\psi}_{sdc}^r e^{-t(\frac{1}{\tau_s} + j\omega_r)} \right] \quad (19)$$

The term $(1/\tau_s)$ can be ignored due to the large time constant of the stator flux. Considering the worst-case scenario, i.e., a phase-to-phase fault, and the worst condition of a full voltage dip ($d = 1$, $\varphi\Psi_0 = \pi$), Ψ_{sdc} is given by

$$\psi_{sdc} = \frac{V_s}{j\omega_s} \quad (20)$$

The amplitudes of the V_{sp} and V_{sn} will be

$$|V_{sp}| = \left(1 - \frac{d}{2}\right) V_s, \quad |V_{sn}| = \frac{d}{2} V_s \quad (21)$$

Substituting Equations (20) and (21) into Equation (19), the rotor EMF caused by the stator flux during asymmetrical faults will be expressed as

$$\vec{e}_r^r = \frac{L_m}{L_s} \left[0.5sV_s e^{j\omega_s t} + 0.5(2-s)V_s e^{-j(2-s)\omega_s t} - (1-s)e^{-t(\frac{1}{\tau_s} + j\omega_r)} \right] \quad (22)$$

The positive-sequence, negative-sequence, and transient components are related to s , $(1-s)$, and $(2-s)$, as can be seen from Equation (22), respectively. Thus, the peak magnitude of the rotor transient EMF is given by

$$|E_r|_{\max} = \frac{L_m}{L_s} V_s [0.5|s| + 0.5(2-s) - (1-s)] \quad (23)$$

Considering the worst-case scenario when $s = -0.3$, the initial amplitude of the rotor EMF can be approximated by Equation (24).

$$|E_r|_{\max-asym} \approx 2.6 \frac{L_m}{L_s} V_s \quad (24)$$

Obviously, the rotor EMF's initial amplitude is high under asymmetrical grid faults, owing to its negative-sequence component. Based on the above analysis and Equations (16) and (24), it is simple to realize that the deepest asymmetrical fault (phase-to-phase) is far more pronounced than the symmetrical fault of the same voltage dip level.

4. Proposed Control Schemes

This section explains the proposed control scheme developed for improving the transient performance of the DFIG. As stated in Section 1, the objectives of this study are to improve the ride-through operation of the DFIG by lowering the transient rotor and stator currents, reducing electromagnetic torque oscillations, and improving the DC-link voltage response. In this context, a combined control of active crowbars employed at the rotor-side and at the DC-link is proposed. A detailed theoretical explanation, designed procedures, mathematical formulations, and analyses of each active crowbar control scheme are provided in this section. A detailed explanation of control systems for RSC and GSC is not included here; however, it can be found in [1,11,17]. The purpose of this study is to investigate the impacts of active crowbars on the transient performance of a wind-driven DFIG system.

4.1. Proposed Control Scheme for LVRT Enhancement

The following subsections provide a detailed discussion and design of the proposed control strategies for facilitating the ride-through operations of the DFIG during grid faults. The primary objectives of an LVRT control strategy are to protect the RSC from

transient currents and the DC-link from overvoltages. The requirements for the successful implementation of the LVRT strategy are as follows:

$$\left. \begin{aligned} |i_r| &\leq 1.5I_{r,rated}, |i_s| \leq 1.5I_{s,rated} \\ 0.85V_{dc-ref} &\leq v_{dc} \leq 1.15V_{dc-ref} \end{aligned} \right\} \quad (25)$$

To satisfy the aforementioned requirements (25) for LVRT, a combination of an active crowbar at the rotor-side and another parallel to the DC-link is proposed and implemented, which is presented in the next subsections. An active crowbar is capable of eliminating the short circuit and allows the device to function normally again when the transient is finished. Active crowbars are commonly employed in the rotor circuit of DFIGs to protect the power converter from the voltage and current transients induced by voltage dips in the power network. As a result, the generator can ride through the fault and quickly resume the operation.

4.1.1. Control Structure of the Crowbar at the Rotor Side

Crowbar protections are designed and installed to safeguard the RSC from overcurrents. The crowbar is activated by isolating the RSC [21] when an aberrant situation is detected; its functionality effectively reduces transient rotor currents. Crowbar activation results in the loss of the controllability of the DFIG because it short-circuits the rotor windings during grid faults to limit the transient current. In this situation, the DFIG receives reactive power from the grid, resulting in DC-link overvoltages. Furthermore, the reduced capacity of the RSC is a key obstacle, as it can handle a limited transient current.

A parallel combination of the RCB and the rotor-crowbar resistors (R_{RCR}) is put in series between the DFIG’s rotor and the RSC. During the steady-state operations, the RCB is connected to the circuit. However, in the event of a fault, the control system trips the RCB and the rotor current starts to flow via R_{RCR} to limit the fault current. This configuration (see Figure 3) has the advantage of allowing for the interrupted control of the DFIG even when the operating conditions are abnormal. To determine the value of R_{RCR} , the following expression is used.

$$R_{RCR} = nR_r \quad (26)$$

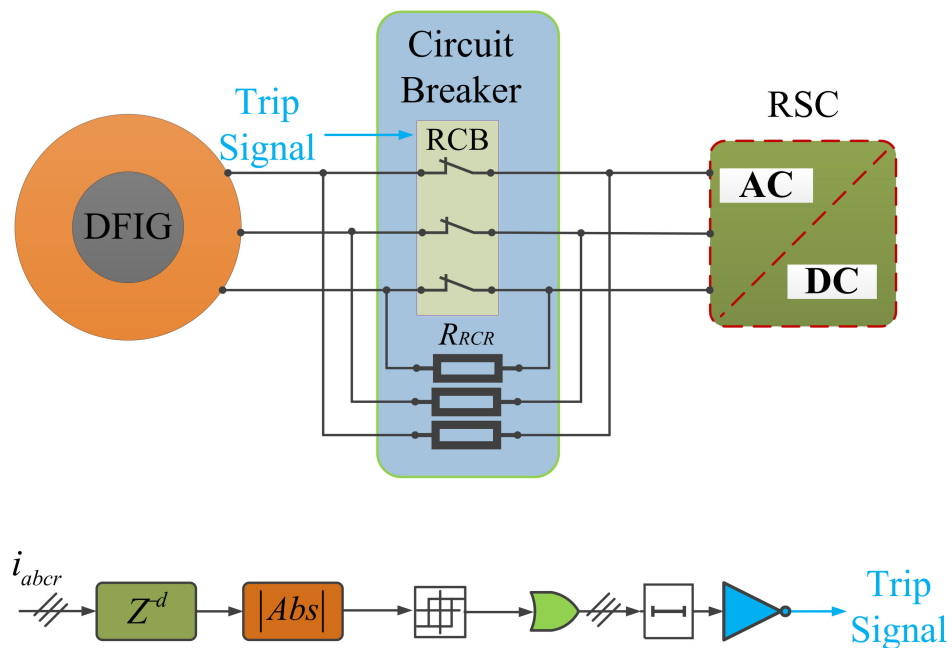


Figure 3. Schematic of the crowbar control system at the rotor side.

Here, n is a multiple of R_r . The R_{RCR} should be carefully chosen, as it has a direct impact on the DFIG's transient performance. It should be high enough to prevent the RSC current from exceeding its limits; however, selecting a value that is too high may increase the transient rotor voltage beyond its acceptable range and cause huge ripples in the DC-link voltage. Therefore, a suitable selection of this resistance is critical. According to [36], 'n' can be between 20 and 50. The total rotor resistance ($R_{r-trans.}$) during the fault becomes

$$R_{r-trans.} = R_r + R_{RCR} = R_r + nR_r = R_r(1 + n) \quad (27)$$

In this context, the transient rotor time constant during faults will be

$$\tau_{r-trans.} = \frac{L_{r-trans.}}{R_{r-trans.}} \quad (28)$$

Here, $L_{r-trans.}$ is the transient rotor inductance and is given by Equation (29).

$$L_{r-trans.} = L_r + \frac{L_s L_m}{L_s + L_m} \quad (29)$$

4.1.2. Control Structure of the Crowbar at the DC-Link

The ultimate objective of integrating the ESDs is the active-power regulation of the system [22]; however, that is outside the focus of this study. This work is limited to the application of an ESD to improve the transient performance of the generator, and this is already available in the literature [22,28]. In this paper, a battery is taken as an ESD. The schematic is presented in Figure 4, which comprises a DC-DC converter and a battery model. The ESD can provide power to the DC-link based on the voltage at the grid side. The type and control scheme of a battery-based ESD affects how well it performs for LVRT enhancement during grid faults. The authors used a battery model from the MATLAB/Simulink library.

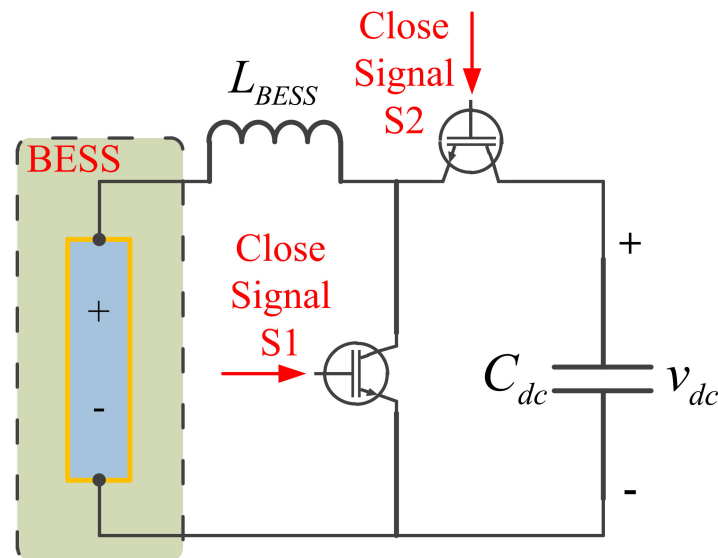


Figure 4. Schematic of a DC-DC converter.

A switching function for activating the switch S1 is defined as

$$\begin{cases} F_s = 1, & v_{dc} < 0.90V_{dc-ref} \\ F_s = 0, & v_{dc} > 0.95V_{dc-ref} \end{cases} \quad (30)$$

Figure 5 depicts the schematic of the crowbar control structure at the DC-link. It has two cascaded PI regulators for voltage and current controls, which track, respectively, the

DC-link voltage (v_{dc}) and ESD current ($i_{bat.}$). To guarantee a consistent DC voltage, the ESD manages the DC-link voltage and regulates the voltage variations by being charged and discharged. The current regulator's output is compared with the carrier waveform (a repeating sequence of a triangle waveform). When exceeding the compared waveform, the output is sent to the switch S1, if $F_s = 1$.

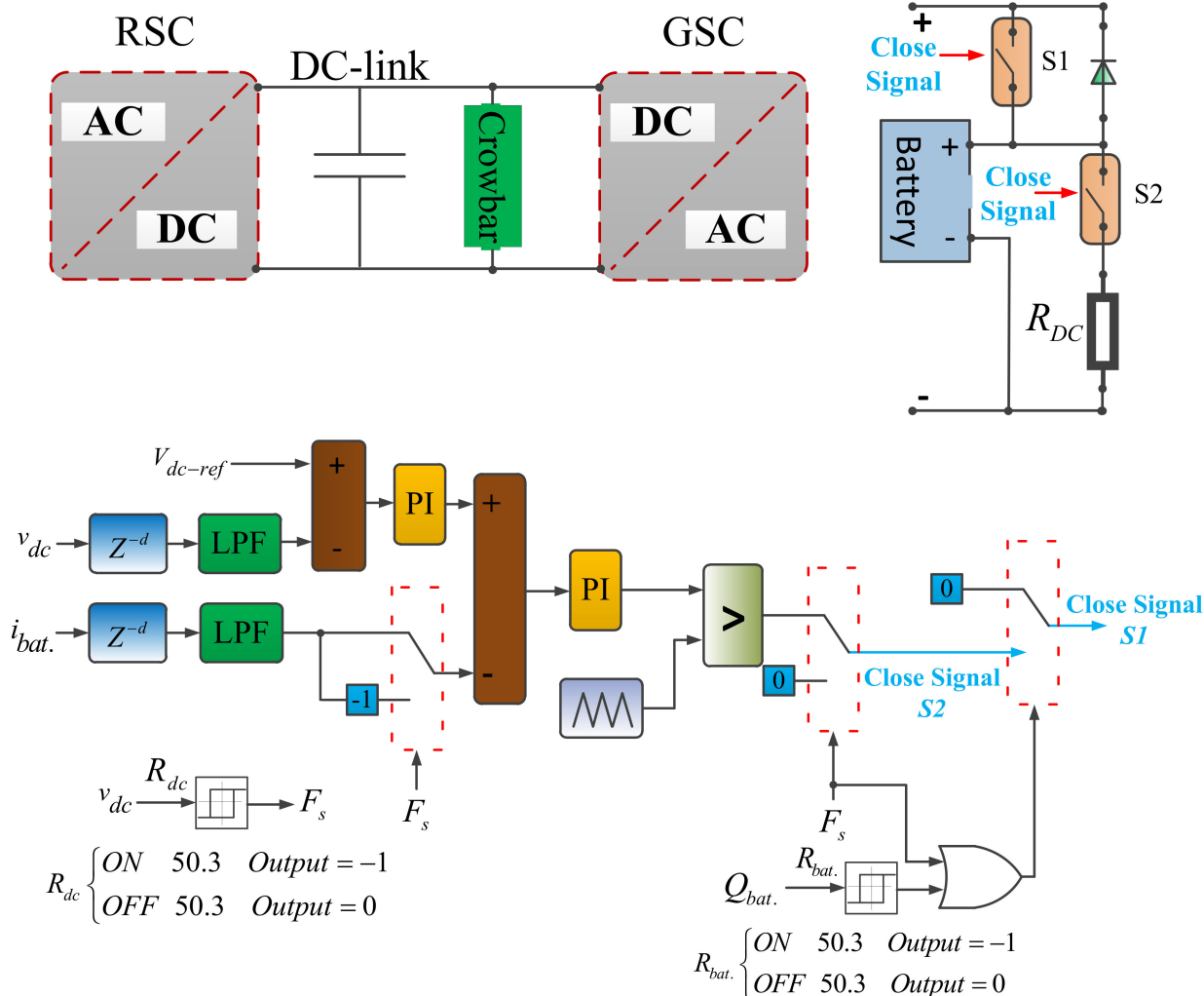


Figure 5. Schematic of the crowbar control system at the DC-link.

The proposed control scheme also realizes the battery-charging process when both of the two conditions are met.

$$F_s = 0, Q_{bat.} < 98\% \tag{31}$$

However, the process can be interrupted at any stage. For a fully charged battery, the state-of-charge will be 100%. Upon fault detection, the ESD will be triggered to provide transient EMF and facilitate voltage regulation.

5. Estimation of the BESS Capacity for LVRT

The ESDs with a sufficient storage capacity are normally installed inside the WECS controls to improve their LVRT capabilities. The energy capacity of an ESD is determined in accordance with the system's power regulation. However, it is beyond the scope of this paper. The emphasis here is on determining the suitable energy capability of an ESD for ancillary control that can firmly support the transient conditions.

The mathematical expression describing the power flow of the DFIG-based WECS is given by

$$P_{grid} = P_{stator} + P_{rotor} \quad (32)$$

In Equation (32), P_{grid} , P_{stator} , and P_{rotor} are the grid-side active power, stator power, and rotor power, respectively. Voltage dips at the grid side impede the delivery of the entire generated output power, resulting in an imbalance in mechanical and electrical torques. Accordingly, the rotor speed will temporarily accelerate during voltage dips, and its peak will depend on d . The over-speeding of the rotor is prevented and compensated for by activating the pitch-angle controller. Furthermore, an increased rotor speed converts a portion of wind energy into mechanical energy, resulting in the rotor KE, which is highly dependent on the wind-speed conditions. The energy flowing through the RSC consists of two parts: (1) energy held in the DC-link and (2) energy transferred to the grid through RSC.

During a severe fault, the P_s is restricted to zero. The required energy capacity of a battery energy storage system (BESS) is estimated as follows

$$\begin{cases} P_{BESS} = P_{rotor} = P_{dc-link} + P_{gsc} \\ E_{BESS} = \int_{t_{start}}^{t_{final}} P_{BESS} \approx \int_{t_{start}}^{t_{final}} P_{dc-link} + \int_{t_{start}}^{t_{final}} P_{gsc} \end{cases} \quad (33)$$

In the above expression, $t_{initial}$ and t_{final} are the instants at which the fault occurs and clears, respectively. The complete expression for assessing the capacity of the BESS can now be computed as

$$E_{BESS} = \frac{1}{2} C_{dc} [v_{dc}^2(t_{final}) - v_{dc}^2(t_{start})] + dV_g I_{gsc,max} [t_{final} - t_{start}] \quad (34)$$

In Equation (34), $I_{gsc,max}$ denotes the maximum current-carrying capacity of the GSC, and V_g is the rated voltage at the point of common coupling. Using the above expression, the basic energy capacity of the BESS is approximated around 140 KW, including some margins, using the parameters given in Appendix A, and $d = 1$ and $(t_{final} - t_{start}) = 0.6$ s are considered.

6. Results and Discussions

This section examines the performance of the control schemes proposed in Section 4 for enhancing the transient performance of a wind-power system during different grid faults and observing their effects on the system. The DFIG parameters were taken from [11]. Simulation studies using MATLAB/Simulink were conducted to highlight the performances of the proposed control schemes.

6.1. Performance of the Proposed Control Scheme for Symmetrical Grid Faults

The system behavior is analyzed by applying a three-phase fault (a step change) on the LV-side of the transformer from 6 s to 6.25 s. Meanwhile, the grid-side voltage, which can be seen in Figure 6a, instantaneously decreases to less than 10% of its normal operating value. Figure 6b–h present the simulation results for the rotor speed, generator torque, DC-link voltage, rotor dq voltage references, stator current, and rotor current, respectively.

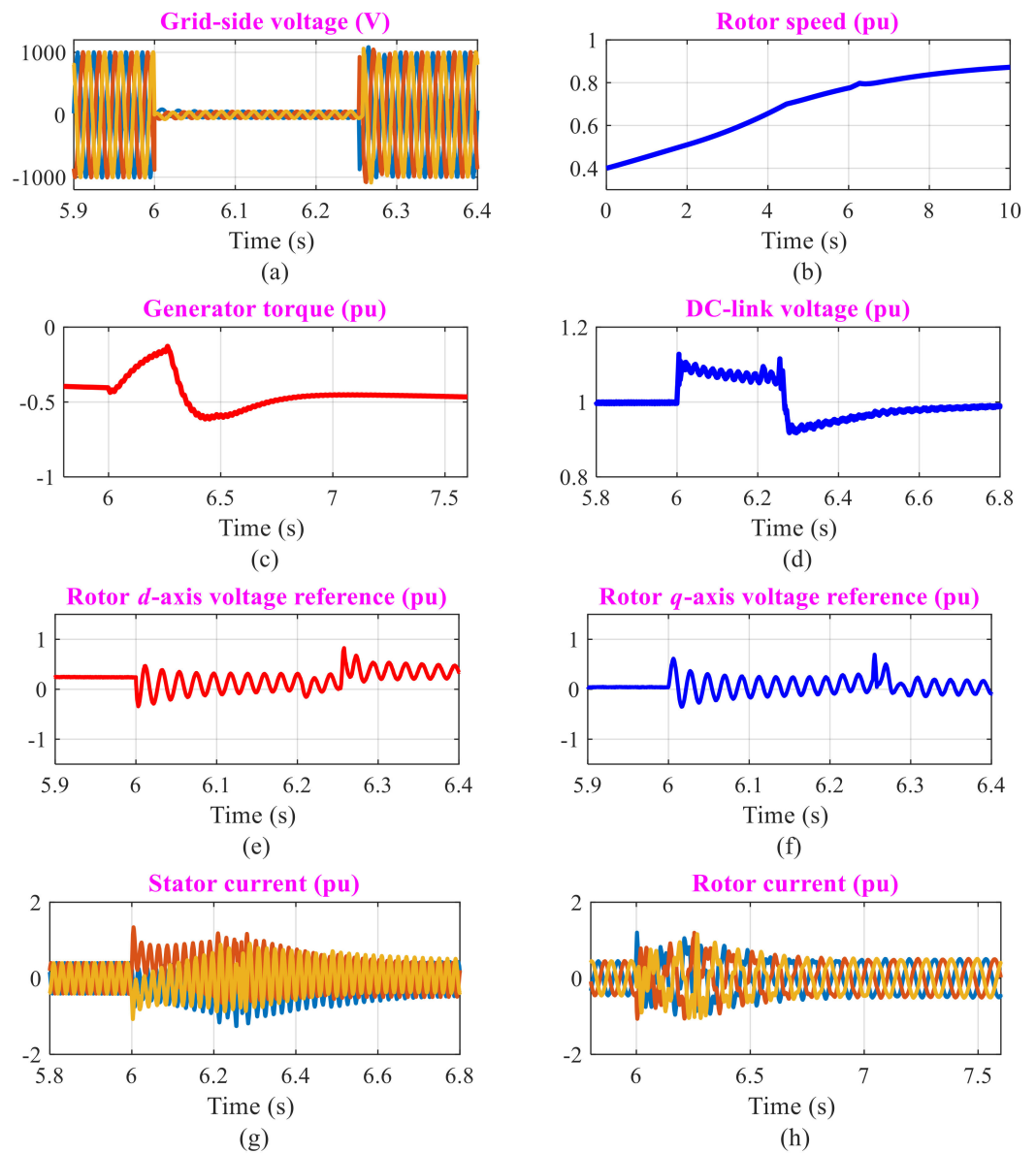


Figure 6. Simulation results of the selected waveforms via the proposed control schemes under symmetrical grid voltage faults.

Figure 6b shows that the effects of the fault on the rotor speed are negligible. The proposed controls efficiently reduce the oscillations of the generator torque, as demonstrated in Figure 6c. Moreover, as seen in Figure 6d, the DC-link voltage fluctuations do not exceed 15% of the rated value, indicating that it remains consistent within limits (25). Similarly, once the fault is cleared, the DC-link voltage drops by no more than 5% of its rated value for a few milliseconds before returning to its rated value. By observing Figure 6e,f, it is evident that the rotor dq voltage references contain transient components both during and after the fault; however, such transients are effectively limited by the proposed control schemes.

The analyses of Figure 6g,h show that the stator- and rotor-current transients are limited to $\pm 50\%$ of their rated values. After the fault is cleared, the acceptable stator and rotor current ranges are also followed. It is noteworthy that during a symmetrical grid fault, there is no possibility of stator- and rotor-current transients during the grid fault, as the activation of active crowbars provides relief by dampening them effectively. Thus, it has been proved that the proposed control schemes successfully implement LVRT operation while significantly reducing the effects of grid disturbances.

6.2. Performance of the Proposed Control Scheme for an Asymmetrical Grid Fault

In this subsection, the implications of an asymmetrical grid fault are discussed, and its impacts on the system are examined. This is accomplished by applying a single-phase-to-ground fault (see Figure 7a) under the same operating conditions as in the prior scenario. The simulation results are used to highlight the behavior of the proposed control method, as shown in Figure 7. However, due to the higher DC stator flux linkage [9], the variations in the selected waveforms (see Figure 7) are higher than for the symmetrical grid fault.

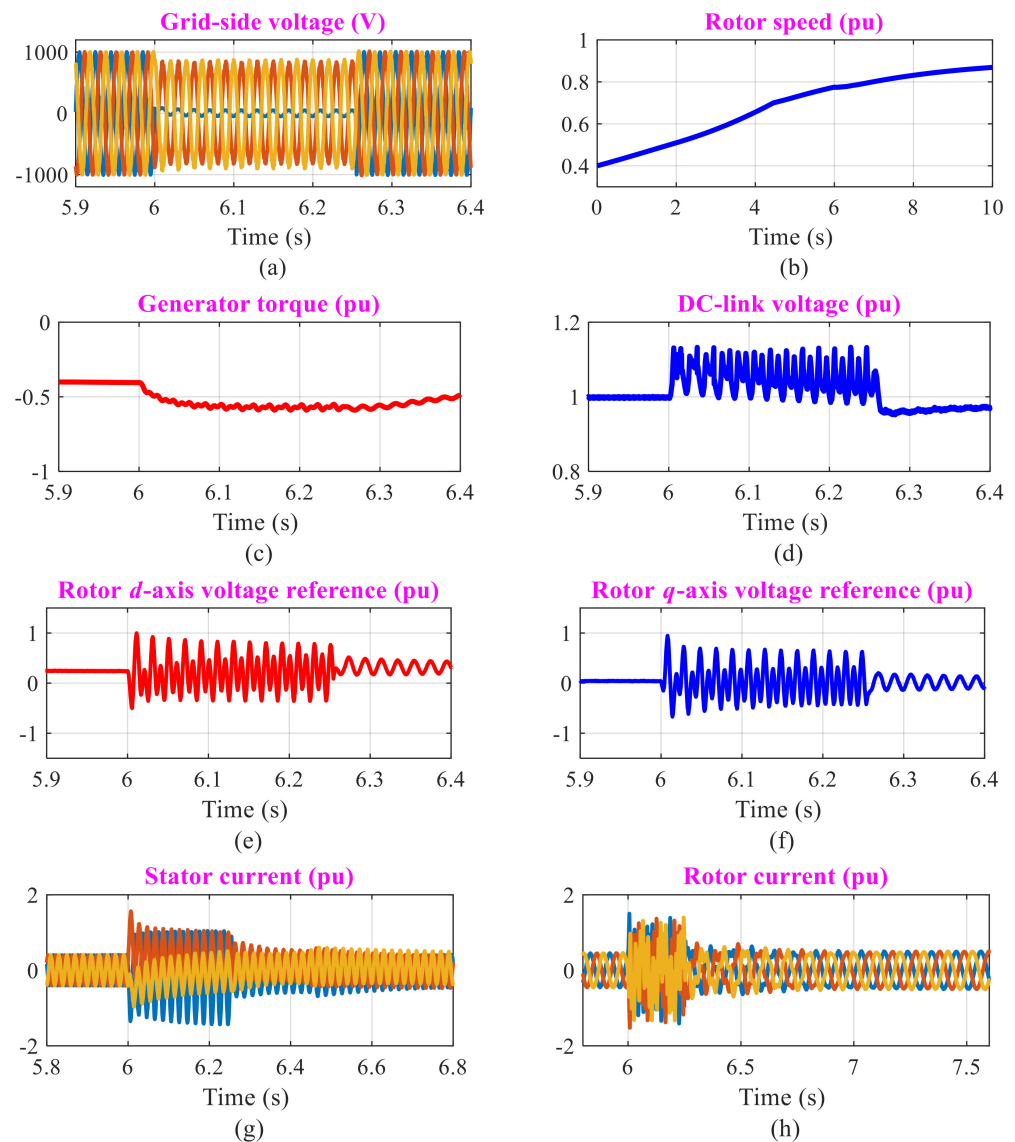


Figure 7. Simulation results of the selected waveforms via the proposed control schemes under asymmetrical grid voltage fault.

From Figure 7d, it can be seen that the transient DC-link overvoltages are limited to 15% above its rated value during the fault. After the fault is cleared, the DC-link voltage drops by no more than 5% of its rated value for a few milliseconds. It implies that the proposed control structure kept the DC-link voltage variations well within their defined performance bounds. The waveforms of the stator and rotor currents are shown in Figure 6g,h. The analyses of these waveforms show that the transient stator and rotor currents are restricted to $\pm 50\%$ of their rated values, and the same measure is fulfilled when the fault is cleared.

It has been noted from the analyses that the system performance using the proposed schemes is significantly improved in terms of reduced levels of transient rotor and stator currents as well as variations in the DC-link voltage, ensuring reliable power-system operation.

6.3. Performance Comparison

Finally, to validate the performance improvement of the proposed design, a comparative study with a DC-chopper is conducted. The system is simulated again for both previously discussed cases, and the same parameters are considered here. The waveforms of the DC-link voltage for symmetrical and asymmetrical grid faults are shown in Figure 8a,b, respectively. The DC-link voltage fluctuations are significantly higher in the case of a DC-chopper compared to the results obtained by the proposed design. The most significant difference is visible after the fault clearance. The DC-link voltage waveforms obtained by the DC-chopper are less than 15% of its rated value. The outcomes demonstrate the superior performance of the designed approach in alleviating the DC-link overvoltages, confirming its worth.

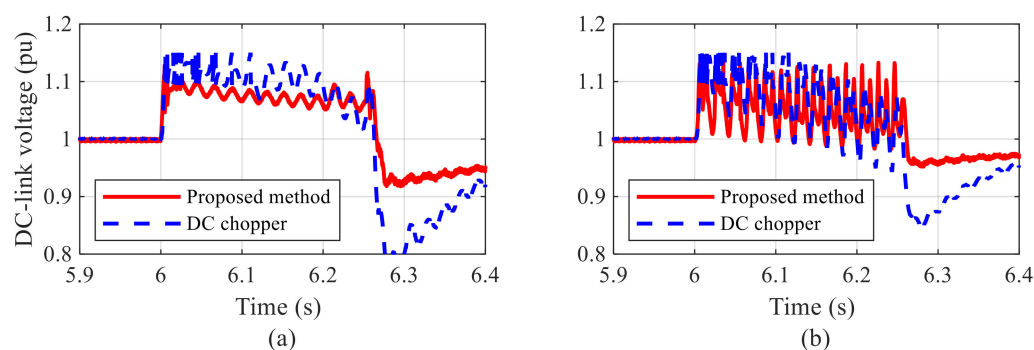


Figure 8. Comparative results: (a) symmetrical grid fault and (b) asymmetrical grid fault.

7. Conclusions

This study addressed the most significant issue—the LVRT capability/transient performance of a DFIG-based WT system when connected to a power grid—and proposed a hardware-based technical solution based on active crowbars. This paper can be concluded as follows:

A combination of active crowbars installed at the rotor side and DC-link was designed and implemented to mitigate the impacts of the grid faults that can destroy the DC-link capacitor and cause massive current stresses on wind-power converters. The results showed that this crowbar combination efficiently controlled the transient rotor and stator currents as well as DC-link voltage variations within permitted limits (25), which were considered the criteria for successful LVRT implementation. Moreover, the electromagnetic torque oscillations were effectively suppressed. Thus, it confirmed the suitability of the proposed design for a DFIG's LVRT functioning and increased the system stability. Finally, the performance of the proposed design was compared to that of a DC-chopper to highlight its superiority under severe system faults.

In the near future, we plan to investigate the performance of the proposed design on the hardware setup and compare it to other start-of-the-art hardware solutions to the problem at hand.

Funding: This research received no external funding.

Institutional Review Board Statement: Not applicable.

Informed Consent Statement: Not applicable.

Data Availability Statement: Data is contained within the article.

Conflicts of Interest: The authors declare no conflict of interest.

Appendix A

Table A1. Parameter of a 1.5 MW DFIG.

Parameter	Value	Unit
Generator rated power	1.5	MW
Rated stator voltage	690	V
Rated frequency	50	Hz
Pole-pair number	2	Nos.
Stator winding resistance	2.65	mΩ
Stator leakage inductance	0.1687	mH
Rotor winding resistance	2.63	mΩ
Rotor leakage inductance	0.1337	mH
Magnetizing inductance	5.4749	mH
Rotational inertia	3	s

References

- Salama, H.S.; Vokony, I. Voltage and Frequency Control of Balanced/Unbalanced Distribution System Using the SMES System in the Presence of Wind Energy. *Electricity* **2021**, *2*, 205–224. [[CrossRef](#)]
- Ali, M.A.S.; Mehmood, K.K.; Kim, C.-H. Full operational regimes for SPMSG-based WECS using generation of active current references. *Int. J. Electr. Power Energy Syst.* **2019**, *112*, 428–441. [[CrossRef](#)]
- Huang, Q.; Zou, X.; Zhu, D.; Kang, Y. Scaled current tracking control for doubly fed induction generator to ride through serious grid faults. *IEEE Trans. Power Electron.* **2016**, *31*, 2150–2165. [[CrossRef](#)]
- Alsmadi, Y.M.; Xu, L.; Blaabjerg, F.; Ortega, A.J.P.; Abdelaziz, A.Y.; Wang, A.; Albataineh, Z. Detailed investigation and performance improvement of the dynamic behavior of grid-connected DFIG-based wind turbines under LVRT conditions. *IEEE Trans. Ind. Appl.* **2018**, *54*, 4795–4812. [[CrossRef](#)]
- Firouzi, M.; Gharehpetian, G.B. LVRT performance enhancement of DFIG-based wind farms by capacitive bridge-type fault current limiter. *IEEE Trans. Sustain. Energy* **2018**, *9*, 1118–1125. [[CrossRef](#)]
- Ali, M.A.S.; Mehmood, K.K.; Baloch, S.; Kim, C.-H. Wind-Speed Estimation and Sensorless Control for SPMSG-Based WECS Using LMI-Based SMC. *IEEE Access* **2020**, *8*, 26524–26535. [[CrossRef](#)]
- Zhu, D.; Zou, X.; Zhou, S.; Dong, W.; Kang, Y.; Hu, J. Feedforward current references control for DFIG-based wind turbine to improve transient control performance during grid faults. *IEEE Trans. Energy Convers.* **2018**, *33*, 670–681. [[CrossRef](#)]
- Haidar, A.M.A.; Muttaqi, K.M.; Hagh, M.T. A coordinated control approach for DC link and rotor crowbars to improve fault ride-through of DFIG-based wind turbine. *IEEE Trans. Ind. Appl.* **2017**, *53*, 4073–4086. [[CrossRef](#)]
- Xiao, S.; Yang, G.; Zhou, H.; Geng, H. An LVRT control strategy based on flux linkage tracking for DFIG-based WECS. *IEEE Trans. Ind. Electron.* **2013**, *60*, 2820–2832. [[CrossRef](#)]
- Zhou, L.; Liu, J.; Zhou, S. Improved demagnetization control of a doubly-fed induction generator under balanced grid fault. *IEEE Trans. Power Electron.* **2015**, *30*, 6695–6705. [[CrossRef](#)]
- Ali, M.A.S.; Mehmood, K.K.; Baloch, S.; Kim, C.-H. Modified rotor-side converter control design for improving the LVRT capability of a DFIG-based WECS. *Electr. Power Syst. Res.* **2020**, *186*, 106403. [[CrossRef](#)]
- Li, X.-M.; Zhang, X.-M.; Lin, Z.-W.; Niu, Y.-G. An improved flux magnitude and angle control with LVRT capability for DFIGs. *IEEE Trans. Power Syst.* **2018**, *33*, 3845–3853. [[CrossRef](#)]
- Majout, B.; Bossoufi, B.; Bouderbala, M.; Masud, M.; Al-Amri, J.F.; Taoussi, M.; El Mahfoud, M.; Motahhir, S.; Karim, M. Improvement of PMSG-based wind energy conversion system using developed sliding mode control. *Energies* **2022**, *15*, 1625. [[CrossRef](#)]
- Morshed, M.J.; Fekih, A. A new fault ride-through control for DFIG-based wind energy systems. *Electr. Power Syst. Res.* **2017**, *146*, 258–269. [[CrossRef](#)]
- Geng, H.; Liu, C.; Yang, G. LVRT capability of DFIG-based WECS under asymmetrical grid fault condition. *IEEE Trans. Ind. Electron.* **2013**, *60*, 2495–2509. [[CrossRef](#)]
- Xie, D.; Xu, Z.; Yang, L.; Østergaard, J.; Xue, Y.; Wong, K.P. A comprehensive LVRT control scheme for DFIG wind turbines with enhanced reactive power support. *IEEE Trans. Power Syst.* **2013**, *28*, 3302–3310. [[CrossRef](#)]
- Ali, M.A.S. Enhanced transient performance of wind-driven PMSG: A revised control structure of wind-power converters. *Adv. Electr. Comput. Eng.* **2022**, *2*, 61–70. [[CrossRef](#)]
- Zhang, Y.; Liu, J.; Zhou, M.; Li, C.; Lv, Y. Double impedance-substitution control of DFIG based wind energy conversion system. *Energies* **2022**, *15*, 5739. [[CrossRef](#)]
- Ma, Y.; Zhu, D.; Zhang, Z.; Zou, X.; Hu, J.; Kang, Y. Modeling and transient stability analysis for Type-3 wind turbines using singular perturbation and Lyapunov methods. *IEEE Trans. Ind. Electron.* **2022**, *70*, 8075–8086. [[CrossRef](#)]

20. Dang, H.P.; Pico, H.N.V. Blackstart and fault ride-through capability of DFIG-based wind turbines. *IEEE Trans. Smart Grid* **2022**, *14*, 2060–2074. [[CrossRef](#)]
21. Jalilian, A.; Naderi, S.B.; Negnevitsky, M.; Hagh, M.T.; Muttaqi, K.M. Controllable DC-link fault current limiter augmentation with DC chopper to improve fault ride-through of DFIG. *IET Renew. Power Gener.* **2017**, *11*, 1304. [[CrossRef](#)]
22. Tabosa da Silva, P.L.; Rosas, P.A.C.; Castro, J.F.C.; Marques, D.d.C.; Aquino, R.R.B.; Rissi, G.F.; Neto, R.C.; Barbosa, D.C.P. Power Smoothing Strategy for Wind Generation Based on Fuzzy Control Strategy with Battery Energy Storage System. *Energies* **2023**, *16*, 6017. [[CrossRef](#)]
23. Rashid, G.; Ali, M.H. Nonlinear control-based modified BFCL for LVRT capacity enhancement of DFIG-based wind farm. *IEEE Trans. Energy Convers.* **2017**, *32*, 284–295. [[CrossRef](#)]
24. Hossain, M.A.; Islam, M.R.; Haque, M.Y.Y.U.; Hasan, J.; Roy, T.K.; Sadi, M.A.H. Protecting DFIG-based multi-machine power system under transient-state by nonlinear adaptive backstepping controller-based capacitive BFCL. *IET Gener. Transm. Distrib.* **2022**, *16*, 4528–4548. [[CrossRef](#)]
25. Padmaja, A.; Shanmukh, A.; Mendu, S.S.; Devarapalli, R.; Serrano González, J.; García Márquez, F.P. Design of capacitive bridge fault current limiter for low-voltage ride-through capacity enrichment of doubly fed induction generator-based wind farm. *Sustainability* **2021**, *13*, 6656. [[CrossRef](#)]
26. Sadi, M.A.H.; AbuHussein, A.; Shoeb, M.A. Transient performance improvement of power systems using fuzzy logic controlled capacitive-bridge type fault current limiter. *IEEE Trans. Power Syst.* **2020**, *36*, 323–335. [[CrossRef](#)]
27. Gounder, Y.K.; Nanjundappan, D.; Boominathan, V. Enhancement of transient stability of distribution system with SCIG and DFIG based wind farms using STATCOM. *IET Renew. Power Gener.* **2016**, *10*, 1171–1180. [[CrossRef](#)]
28. Shen, Y.W.; Ke, D.P.; Sun, Y.Z.; Kirschen, D.S.; Qiao, W.; Deng, X.T. Advanced auxiliary control of an energy storage device for transient voltage support of a doubly fed induction generator. *IEEE Trans. Sustain. Energy* **2016**, *7*, 63–76. [[CrossRef](#)]
29. Wessels, C.; Gebhardt, F.; Fuchs, F.W. Fault ride-through of a DFIG wind turbine using a dynamic voltage restorer during symmetrical and asymmetrical grid faults. *IEEE Trans. Power Electron.* **2011**, *26*, 807–815. [[CrossRef](#)]
30. Wang, X.; Peng, L. Dynamic voltage equalization control of D-STATCOM under unbalanced grid faults in low-voltage network. *IEEE Trans. Power Electron.* **2022**, *38*, 2384–2397. [[CrossRef](#)]
31. Xiao, F.; Xia, Y.; Zhang, K.; Zhang, Z.; Yin, X. Fault characteristics analysis of DFIGWT in whole LVRT process considering control strategy switching between RSC and crowbar. *Int. J. Electr. Power Energy Syst.* **2023**, *145*, 108615. [[CrossRef](#)]
32. Blaabjerg, F.; Xu, D.; Chen, W.; Zhu, N. *Advanced Control of Doubly Fed Induction Generator for Wind Power Systems*; Wiley-IEEE Press: Piscataway, NJ, USA, 2018.
33. Abad, G.; Lopez, J.; Rodriguez, M.; Marroyo, L.; Iwanski, G. *Doubly Fed Induction Machine: Modeling and Control for Wind Energy Generation*; Wiley-IEEE Press: Piscataway, NJ, USA, 2011.
34. Wu, B.; Lang, Y.; Zargari, N.; Kouuro, S. *Power Conversion and Control of Wind Energy Systems*; Wiley-IEEE Press: Piscataway, NJ, USA, 2011.
35. Muller, S.; Deicke, M.; De Doncker, R.W. Doubly fed induction generator systems for wind turbines. *Ind. Appl. Mag.* **2002**, *8*, 26–33. [[CrossRef](#)]
36. Noubrik, A.; Chrifi-Alaoui, L.; Bussy, P.; Benchaib, A. Analysis and simulation of a crowbar protection for DFIG wind application during power systems disturbances. *J. Mech. Eng. Autom.* **2011**, *1*, 303–312.

Disclaimer/Publisher’s Note: The statements, opinions and data contained in all publications are solely those of the individual author(s) and contributor(s) and not of MDPI and/or the editor(s). MDPI and/or the editor(s) disclaim responsibility for any injury to people or property resulting from any ideas, methods, instructions or products referred to in the content.